High-speed camera with real time processing for frequency domain imaging

Victor Shia,[1] David Watt,[2] and Gregory W. Faris[1,*]

[1]*Physical Sciences Division, SRI International, 333 Ravenswood Avenue, Menlo Park, CA 94025, USA*
[2]*Engineering& Systems Group, SRI International, 333 Ravenswood Avenue, Menlo Park, CA 94025, USA*
**gregory.faris@sri.com*

Abstract: We describe a high-speed camera system for frequency domain imaging suitable for applications such as in vivo diffuse optical imaging and fluorescence lifetime imaging. 14-bit images are acquired at 2 gigapixels per second and analyzed with real-time pipeline processing using field programmable gate arrays (FPGAs). Performance of the camera system has been tested both for RF-modulated laser imaging in combination with a gain-modulated image intensifier and a simpler system based upon an LED light source. System amplitude and phase noise are measured and compared against theoretical expressions in the shot noise limit presented for different frequency domain configurations. We show the camera itself is capable of shot noise limited performance for amplitude and phase in as little as 3 ms, and when used in combination with the intensifier the noise levels are nearly shot noise limited. The best phase noise in a single pixel is 0.04 degrees for a 1 s integration time.

OCIS codes: (170.0110) Imaging systems; (170.3880) Medical and biological imaging; (170.6920) Time-resolved imaging; (170.5280) Photon migration; (170.3650) Lifetime-based sensing.

References and links

1. B. Chance, M. Cope, E. Gratton, N. Ramanujam, and B. Tromberg, "Phase measurement of light absorption and scatter in human tissue," Rev. Sci. Instrum. **69**(10), 3457–3481 (1998).
2. E. M. Sevick, B. Chance, J. Leigh, S. Nioka, and M. Maris, "Quantitation of time- and frequency-resolved optical spectra for the determination of tissue oxygenation," Anal. Biochem. **195**(2), 330–351 (1991).
3. S. J. Madsen, E. R. Anderson, R. C. Haskell, and B. J. Tromberg, "Portable, high-bandwidth frequency-domain photon migration instrument for tissue spectroscopy," Opt. Lett. **19**(23), 1934–1936 (1994).
4. H. Jiang, K. D. Paulsen, U. L. Osterberg, B. W. Pogue, and M. S. Patterson, "Simultaneous reconstruction of optical absorption and scattering maps in turbid media from near-infrared frequency-domain data," Opt. Lett. **20**(20), 2128–2130 (1995).
5. M. Gerken and G. W. Faris, "High-precision frequency-domain measurements of the optical properties of turbid media," Opt. Lett. **24**(14), 930–932 (1999).
6. V. Toronov, E. D'Amico, D. Hueber, E. Gratton, B. Barbieri, and A. Webb, "Optimization of the signal-to-noise ratio of frequency-domain instrumentation for near-infrared spectro-imaging of the human brain," Opt. Express **11**(21), 2717–2729 (2003).
7. A. B. Thompson and E. M. Sevick-Muraca, "Near-infrared fluorescence contrast-enhanced imaging with intensified charge-coupled device homodyne detection: measurement precision and accuracy," J. Biomed. Opt. **8**(1), 111–120 (2003).
8. S. V. Patwardhan and J. P. Culver, "Quantitative diffuse optical tomography for small animals using an ultrafast gated image intensifier," J. Biomed. Opt. **13**(1), 011009 (2008).
9. T. French, J. Maier, and E. Gratton, "Frequency domain imaging of thick tissues using a CCD," Proc. SPIE **1640**, 254–261 (1992).
10. J. R. Lakowicz and K. W. Berndt, "Lifetime-selective fluorescence imaging using an rf phase-sensitive camera," Rev. Sci. Instrum. **62**(7), 1727–1734 (1991).
11. R. A. Colyer, C. Lee, and E. Gratton, "A novel fluorescence lifetime imaging system that optimizes photon efficiency," Microsc. Res. Tech. **71**(3), 201–213 (2008).
12. K. Zhang and J. U. Kang, "Real-time intraoperative 4D full-range FD-OCT based on the dual graphics processing units architecture for microsurgery guidance," Biomed. Opt. Express **2**(4), 764–770 (2011).
13. A. E. Desjardins, B. J. Vakoc, M. J. Suter, S. H. Yun, G. J. Tearney, and B. E. Bouma, "Real-time FPGA processing for high-speed optical frequency domain imaging," IEEE Trans. Med. Imaging **28**(9), 1468–1472 (2009).

#146883 - $15.00 USD Received 2 May 2011; revised 13 Jun 2011; accepted 13 Jun 2011; published 15 Jun 2011

14. J. R. Janesick, "Scientific Charge-Coupled Devices," (SPIE Press, Bellingham, Washington, 2001), pp. 101–105.
15. D. F. Walls, "Squeezed states of light," Nature **306**(5939), 141–146 (1983).
16. X. Gu, K. Ren, and A. H. Hielscher, "Frequency-domain sensitivity analysis for small imaging domains using the equation of radiative transfer," Appl. Opt. **46**(10), 1624–1632 (2007).
17. T. Tu, Y. Chen, J. Zhang, X. Intes, and B. Chance, "Analysis on performance and optimization of frequency-domain near-infrared instruments," J. Biomed. Opt. **7**(4), 643–649 (2002).

1. Introduction

The frequency domain technique [1] is a method commonly used to perform time-resolved measurements for biomedical optics applications. Temporal resolution is achieved by measuring the phase shift of a sinusoidally modulated light source. An advantage of frequency domain measurements is that the phase shift can typically be measured to a very small fraction of the optical period (on the order of a part in 10^4), which means that a frequency domain system can achieve better temporal resolution than a time domain system with the same bandwidth. The two primary applications of frequency domain imaging are diffuse imaging in vivo and fluorescence lifetime imaging. For diffuse optical imaging, the time-resolved measurements are used to separate the contributions of scatter and absorption, hence improving the ability to recover information on concentrations of endogenous chromophores such as hemoglobin concentrations and hemoglobin oxygenation. For fluorescence lifetime imaging, the lifetime information can be used to provide information on the environment of the emitting fluorophor such as pH, oxygen concentrations, or ion concentrations through fluorescence quenching, molecular reorientation, or proximity of neighboring chromophores through fluorescence resonance energy transfer (FRET). The phase noise is often the critical performance criterion for these applications.

A variety of methods have been applied to frequency domain measurements including both single channel or point measurements [2–6] with either homodyne and heterodyne detection and imaging systems [7–11], which generally use heterodyne detection. Imaging systems have been described with application to both photon migration or diffuse imaging [7–9] and fluorescence lifetime imaging (FLIM) [10,11]. The imaging systems typically acquire images at different phases and process the images on a desktop computer. We demonstrate a different approach using a high-speed camera with real-time processing performed by field programmable gate arrays (FPGAs). This enables increasing the intermediate frequency by roughly 2 orders of magnitude from ~10 Hz to ~1 kHz and enables calculation amplitude and phase images at this frame rate in real time.

Higher frame rates and higher intermediate frequencies provide a number of potential advantages for frequency domain imaging. When performing measurements at low frame rates or low intermediate frequencies, the phase results can be impacted by system phase drift or 1/f noise. Higher frame rates and higher intermediate frequencies can reduce errors from such phase instability on the final phase results. Faster frame rates enable performing more phase measurements in the same total image integration time, which also improves phase results when the light source has amplitude instabilities or nonlinearities. The faster frame rates can also be used to capture more rapidly changing features in images such as kinetic changes in lifetimes for FLIM or cardiac or respiratory cycles in diffuse optical imaging. Finally, a higher frame rate can also support more sophisticated frequency coding, which can include using multiple frequencies for FLIM to recover lifetime information from more complex systems, or using wavelength to frequency encoding (i.e., each wavelength has a different modulation frequency) to allow simultaneous measurements of multiple wavelengths with a single detector for either FLIM or diffuse imaging.

One challenge in high-speed imaging is storing all of the data, which is typically retained in the camera memory and downloaded to the computer for data processing once the data set is complete. For this system we stream the images to computer for pipeline processing in FPGAs, so camera memory limitations are avoided. After image processing, the raw data (quadrature images) are discarded and only the processed images are retained, which include the AC amplitude, phase, and DC amplitude images. In the process the total data bandwidth can be reduced greatly by factors of as much of 100 from around 1 kHz around 10 Hz.

#146883 - $15.00 USD Received 2 May 2011; revised 13 Jun 2011; accepted 13 Jun 2011; published 15 Jun 2011

FPGAs are a type of integrated circuit with an array of programmable logic components or logic blocks coupled by programmable interconnects. The FPGAs processing architecture performs parallel computations using multiple processors, enabling extremely high processing speed. Graphical processing units (GPUs) are another type of parallel processors that also allow very high processing speed. However, since GPUs do not provide capabilities for data input at the very high data input rates we require, FPGAs are the only option for this application. Both FPGAs and GPUs have been applied to processing of Fourier domain optical coherence tomography images [12,13].

We describe the system design considerations and how they guide the imaging system architecture. System performance is tested using both an RF-modulated laser with image intensifier and with an LED source. The results are compared with theoretical expressions for shot-noise-limited performance, which are presented in the appendix. With the LED source we obtained shot-noise-limited results in as little as 3 ms. The laser system provides results close to the shot-noise-limit. A shot noise limited system is desired because it means that the system itself introduces no noise.

2. Instrumentation

2.1. Camera and data processing

The imaging system is based on a high speed CMOS camera (Vision Research Phantom v7.3 w/ RTO real-time output) and field programmable gate array (FPGA) boards for high-speed data processing. Diagrams of the overall system and the FPGA architecture are shown in Figs. 1 and 2, respectively. The camera can acquire 14-bit images at 6800 frames per second with resolution up to 800x600 pixels. The FPGA boards, purchased from Nallatech, comprise a BenNUEY-PCI-2V3000-4 PCI motherboard with three FPGA module boards: a BenDATA-II 2VP70-6 to receive the data from the camera and two BenDATA-WS 2V6000-4 boards for processing and image caching. All boards are based on Xilinx Virtex-II and Virtex-II Pro (for 2VP70-6) FPGAs.

High-speed cameras typically store all images in memory on the camera. This camera is configured with real-time output, for which FPGAs in the camera stream the data to another device at up to 8Gb/s through a MPO/MTP 12-fiber multichannel cable. The streaming data is converted from optical digital signals to electrical digital signals with a Zarlink ZL60102 parallel fiber receiver module on a custom board designed at SRI. This board includes a LV7744DV 106.25 MHz oscillator, which matches the 212.5 MB/s (post 8b/10b decoding) or 2.125 Gb/s (pre 8b/10b decoding) data rate per fiber channel from the camera. The electrical signals are subsequently transferred to Rocket I/O multi-gigabit transceivers on the BenData-II board FPGAs using Samtec QSE/QTE high-speed differential pair board-to-board connections with the 106.25 MHz oscillator as an external reference. Receiver code modified from code provided by Vision Research is used to reassemble the data in the BenData-II. The reassembled data is split into two streams sent to the two BenData-WS boards for calculations. The FPGA processors on the BenData-WS boards calculate two quadrature values, which we denote as X and Y, as well as the DC level, D, for each pixel. After the data processing, the two FPGA processors stream the data to the BenNUEY motherboard, which concatenates the data and outputs it to the PC through the 64-bit PCI interface.

The X and Y quadratures are calculated as the correlation between each pixel data value and cosine and sine waveforms according to the equations

$$X = \sum_{n=0}^{K-1} S(n\Delta t)\cos(\omega n\Delta t + \gamma)\Delta t \quad \text{and} \quad Y = \sum_{n=0}^{K-1} S(n\Delta t)\sin(\omega n\Delta t + \gamma)\Delta t \qquad (1)$$

where $S(t) = S_{DC}\,[1 + m_1\cos(\omega t + \alpha)]$ is the optical signal and S_{DC} is the DC signal on a given pixel in counts per second. A third value, the accumulated DC value, $D = S_{DC}\, n\Delta t$, is calculated by summing the pixel counts without a sinusoid multiplier. Three 16-bit words are stored for each pixel representing the accumulated DC value, D, and the two quadratures, X and Y. Calculation of the correlations of Eq. (1) do not require storage of the individual

#146883 - $15.00 USD Received 2 May 2011; revised 13 Jun 2011; accepted 13 Jun 2011; published 15 Jun 2011

signals at each time point $S(n\Delta t)$, only the running summation of the product of the pixel counts and the sinusoid. The FPGA discards the rest of the image data, converting gigabytes of image data to 8 Mb/image for 800x600 pixels, each 16 bits deep. The FPGA boards were specified primarily based on the data transfer rates and onboard memory. The 8 Rocket I/O inputs support 212.5 MB/s per channel for total bandwidth of 1700 MB/s. The adjacent bus between the BenData-II and the two BenDATA-WS boards supports 64-bit inputs at 66 MHz for a total of 1056 MB/s for both paths. The smaller data rate of the two (1056 MB/s) supports 16 bit processing of full camera frames at 1000 frames/s or 8-bit images at 2000 frames/s. Each BenDATA-WS provides up to 24 MB wide ZBT SRAM for a total of 48 MB, exceeding the maximum storage of 24 MB for the three images – the DC image and the two AC quadrature images.

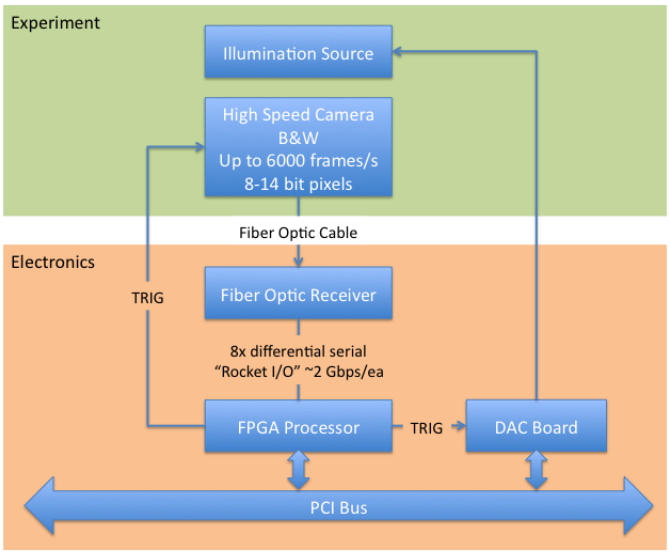

Fig. 1. Schematic of optical and electrical circuits.

Two quadrature illumination waveforms are provided by the analog outputs of National Instruments PCI PCI-6711 12-bit analog output DAQ board. Timing is provided through a SCSI connector on the backplate of the BenNUEY, providing the frame clock to the Phantom camera, resetting the illumination waveform on the DAQ board, and clocking the illumination waveform. Data acquisition is performed using Labview, although the loading of the FPGA code is performed with a call to MATLAB. Data analysis is performed in MATLAB.

Once the desired integration time is complete, the AC amplitude, A, and phase, ϕ, are calculated according to Eq. (2) and Eq. (3)

$$A = \left(X^2 + Y^2\right)^{1/2}, \tag{2}$$

$$\phi = \tan^{-1}\left(X / Y\right). \tag{3}$$

We have tested the imaging system performance using two conditions: (1) high frequency imaging (100 MHz) using a laser and image intensifier for heterodyne downconversion and (2) low frequencies (50 to 333 Hz) using an LED.

2.2 RF electronics

High frequency imaging at 100 MHz was performed using a laser and image intensifier using circuitry shown in Fig. 3. The primary RF source is a 100 MHz signal produced by a

#146883 - $15.00 USD Received 2 May 2011; revised 13 Jun 2011; accepted 13 Jun 2011; published 15 Jun 2011

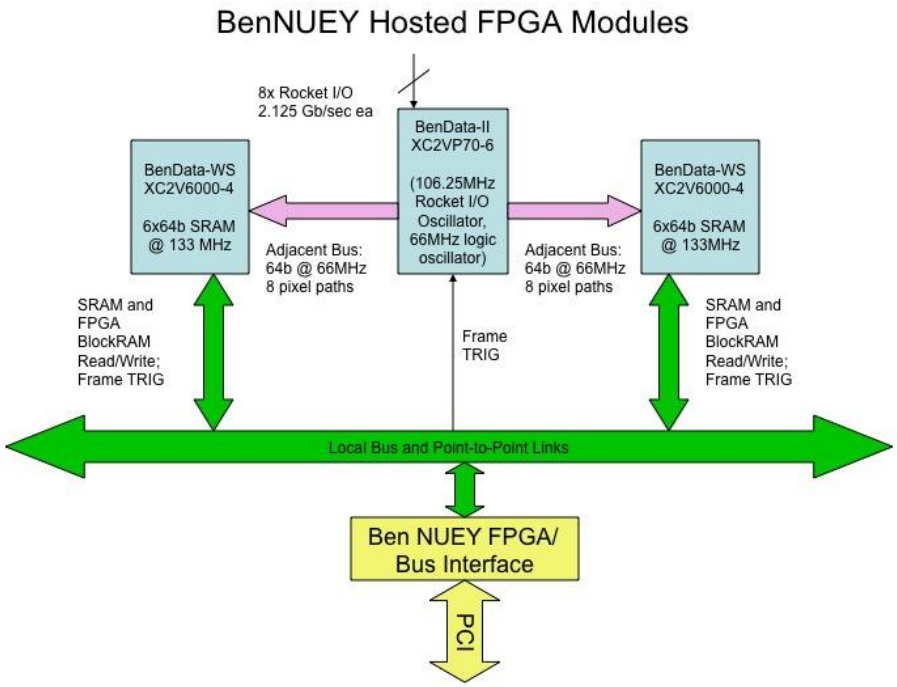

Fig. 2. Schematic of signal flow on FPGA boards.

Wilmanco VS-C-100 oscillator and is split with one portion modulating the photocathode of the image intensifier, and the other sent to the IQ modulator. The National Instruments PCI 6711 DAQ board provides two 10-333 Hz sinusoid signals in quadrature to the IQ modulator, which mixes them with the 100 MHz signal to create the 100+ MHz signal. The 100+ MHz signal is added to a dc bias voltage to drive the laser diode. The 100 MHz signal is amplified using a Kalmus Engineering model 250c RF amplifier providing ~60 V_{rms}, which is applied to the image intensifier photocathode through a bias tee. The low frequency image (1-333 Hz) signal is created by the heterodyne mixing of the 100 MHz and 100+ MHz signal, which produces the low frequency signal and a high frequency signal at 200 MHz. The 200 MHz is filtered by the phosphor screen in the image intensifier, which acts as a low pass filter. The low frequency signal is projected onto the phosphor screen, which is captured by the high-speed camera.

3. System performance

The system produces three output images: a DC image, and AC image, and a phase image. Examples of these for illumination using an LED are shown in Fig. 4.

3.1 Assessment of phase precision and linearity

The phase is a critical performance parameter for frequency domain imaging. We have assessed whole-image phase precision and linearity of the LED and the image intensifier setups. For the image intensifier setup, the laser uniformly illuminated the intensifier photocathode and the intensifier phosphor screen was imaged onto the camera with a Nikon 60mm f/2.8D AF Micro-Nikkor lens. The parameters for the tests are summarized in Table 1. For the LED we were able to operate the camera at the maximum frame rate for 800x600 14-bit images at 1000 Hz and a maximum modulation frequency of 333 Hz. Because of the limited light available from the intensifier phosphor screen, a longer exposure time (2.4 ms) was used, limiting the frame rate to 400 Hz. Using a tapered fiber bundle instead of a lens

#146883 - $15.00 USD Received 2 May 2011; revised 13 Jun 2011; accepted 13 Jun 2011; published 15 Jun 2011

would improve the coupling efficiency between the intensifier and the camera and allow shorter integration times and faster frame rates with the intensifier. The camera's frame rate can be increased to at least 2000 Hz with the new generation of BenNUEY FPGAs.

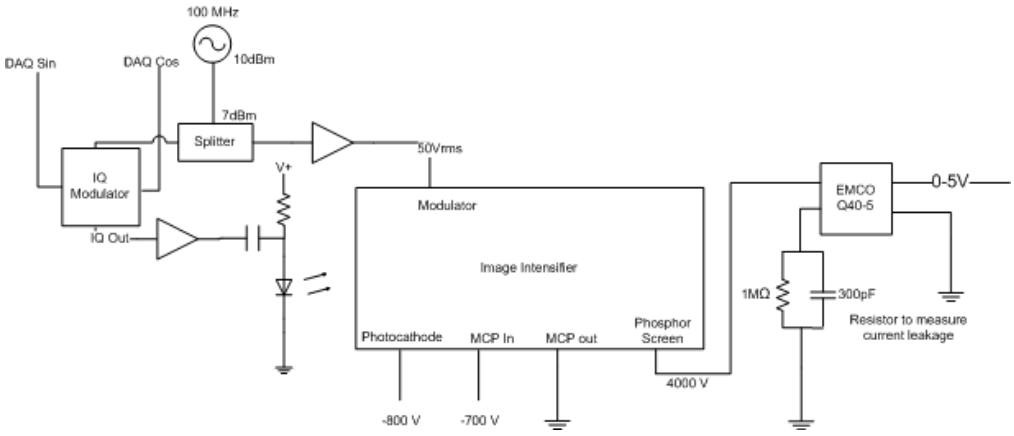

Fig. 3. Schematic of RF circuitry.

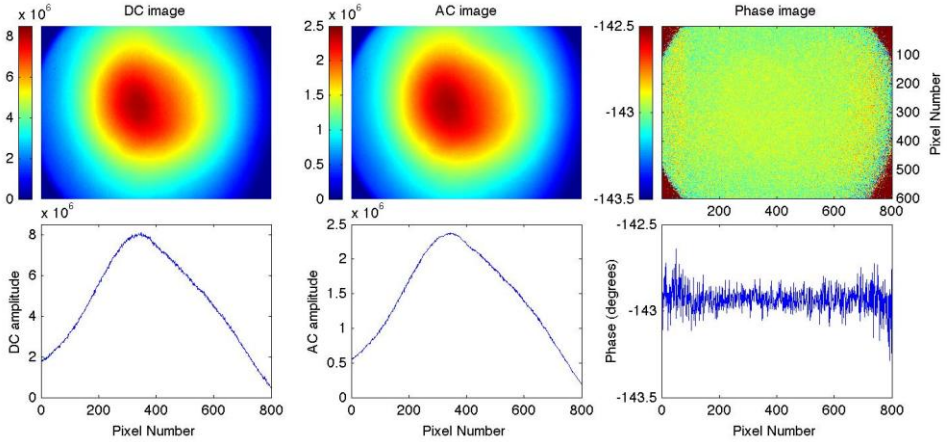

Fig. 4. Examples of DC image, AC image, and phase image using LED illumination. The graphs under each image show the pixel counts at row 300. The units of the DC and AC images are the summation of the pixel counts from each image. Using a range of intensities in a single image is useful for studying the limiting noise behavior as described below.

For each setup, the light source to the camera was modulated at a frequency between 10 to 250 Hz. In the setup described by Fig. 3, the intensifier gain was held constant for each trial. Measurement precision relied on four system parameters (1) the number of frames per cycle taken, (2) the number of cycles, (3) camera frame rate, and (4) the camera exposure time. Data acquisition parameters were chosen such that acquisition time totaled either 1 second, acquired with both LED and intensifier setups (Tables 2 and 3) or less than 10 ms, acquired with the LED only (Table 4). Longer acquisition times are typical for applications where low light levels are available, while short acquisition times can be used for applications when more light is available.

Table 1. Parameters for System Tests using LED and Laser

	Frame Rate (Hz)	Exposure (μs)	Modulation Depth		Phase increment (degrees)
			Optical	Electrical	
LED	1000	200	$m_1 = 0.6$	-	1
Laser	400	2400	$m_1 = 1$	$m_2 = 0.3$	5

#146883 - $15.00 USD Received 2 May 2011; revised 13 Jun 2011; accepted 13 Jun 2011; published 15 Jun 2011

Table 2. Linearity measurements for LED image data taken over 1s with LED phase changes (α) and FPGA phase changes (γ)

Frames Per Cycle	4		5		10	20
Cycles or Frequency	250		200		100	50
Phase Varied	α	γ	α	γ	α	α
Linearity	1.0001	1.0000	1.0000	1.0000	1.0000	0.9999
Residual (deg)	0.2221	0.0010	0.0304	0.0008	0.0193	0.0176
Phase in image (deg)	0.0906	0.1300	0.0851	0.1142	0.0628	0.0503

Table 3. Linearity measurements for image intensifier data taken over 1s

Frames Per Cycle	20
Cycles or Frequency	20
Linearity	0.9983
Residual (deg)	0.2851
Phase in image (deg)	0.8790

Table 4. Linearity measurements for LED image data taken at ≤ 10ms

Frames Per Cycle	3	4	5	6	7	8	10
Cycles	1	1	1	1	1	1	1
Frequency (Hz)	333.3	250	200	166.7	142.9	125	100
Linearity	0.9992	0.9995	1.0000	1.0005	0.9999	0.9997	0.9999
Residual (deg)	0.0226	0.017	0.0159	0.013	0.0180	0.0125	0.0109
Phase in image (deg)	0.8124	0.6344	0.5776	0.5254	0.4884	0.4581	0.4123

3.2 Results of system linearity

Phase linearity was characterized using two values: the actual linearity and residual of measurements, each calculated from values averaged over 5 trials. As the phase between the illumination waveform and the correlation waveform is varied, we expect the image phase should change proportionally. Fitting a line to the output phase as a function of the phase difference between the illumination and correlation waveforms gives a value of 1 to within 0.1% or better for the LED and 0.2% for the laser/intensifier (see row labeled linearity in Tables 2-4). The standard deviation between the phase measurements and this line is given as the second line (residual) in Tables 2-4. From Table 2 we see that there is a large difference in the residual depending on whether we vary the phase of the illumination waveform (α, following the notation in the Appendix) or the correlation (detection) waveform, γ, for 4 frames per cycle. This is believed to be due to nonlinearity of the DAQ-driven LED power, which leads to a different apparent phase depending the exact phase, α, of the sinusoid when the light level is produced. This effect can be avoided by using more frames per cycle or presumably though generation of a voltage waveform that corrects for the LED nonlinearity. When the nonlinearity is avoided, the residual is 0.02 or better for the LED and 1 s integration time and ~0.3 for the intensifier. All of the data in Tables 3 and 4 use variation of the detection waveform phase, γ, for which there is no nonlinearity and no linearity bias. The final parameter in Tables 2-4 is the variation in phase across the image (phase in image). This value is on the order of 0.1 degree for the LED and an integration time T = 1 s, but drops to around 0.5-1 degree for T < = 10 ms. The laser/intensifier has worse performance, or 0.9 degree for T = 1 s.

#146883 - $15.00 USD Received 2 May 2011; revised 13 Jun 2011; accepted 13 Jun 2011; published 15 Jun 2011

3.3 Results of system precision

Phase precision was measured using the noise variation in DC, AC and phase for each pixel across 30 images with the same parameters. The standard deviation and mean for each pixel over the 30 images were calculated. The measured error was then plotted against the theoretical noise calculated using the system's photon transfer curve, which was obtained using standard methods for both setups. Using the Photon Transfer Curve method described in [14], the gain for the camera system was 0.65 counts/electron when the slope of the standard deviation vs mean plot was about 0.35. The gain was calculated by finding the ratio of the DC signal variance to the DC signal within an image. For the laser diode, we calculated the gain of the laser diode system using the expressions in Table 7 to relate AC signal variance to the AC signal. The calculated gain was approximately 1.2 when the slope of the standard deviation vs mean plot was 0.52. Using the calculated gain values, the theoretical noise values were calculated (using the equations in the appendix) and compared to actual noise from these measurements. All measurements were done with phase differences ranging from −180 to 180 degrees in 5-degree increments. 50 images were taken at each phase and only the last 30 were used for measurements.

For LED data with an integration time of 1 second, the DC noise is higher than shot noise while AC and phase noise follow shot-noise theorized values (Fig. 5). The extra noise in the DC measurements may be attributed to the integration of 1/f noise over 1000 frames. According to Fig. 5, the AC and phase noise both approach the shot noise limit as the amplitude increases beyond an average pixel AC amplitude of 100 counts for a single frame (or 10^5 counts for 1000 frames) out of a maximum of 2^{14} counts for the 14-bit images.

For 4 to 10 frames in a single cycle using the LED, the measured DC, AC and phase noises all reach the theorized shot noise limit as the signal amplitude increases. For images with 3 frames in a single cycle, the AC noise appears to be below the shot noise limit and the phase noise is above the shot noise limit (Fig. 6). Three frames per cycle, the theoretical minimum number of points needed to determine a sinusoid with unknown DC offset, AC amplitude and frequency, is a special case which will be discussed later with Fig. 8.

The laser diode data was not as ideal and did not meet the theoretical shot-noise calculations. Using the gain calculated from the AC measurements, AC and phase noise are slightly above the shot-noise values and the DC noise is very noisy and seems to be dependent on the phase difference between the laser and the correlation waveform (Fig. 7). However, the slope of all the noise plots does approach that of the theoretical slopes. Part of the DC noise may be attributed to the integration of 1/f noise over 400 frames and an unstable image intensifier.

3.4 AC/DC amplitude results

We can compare the AC/DC amplitude ratio with the theoretical expressions from Table 7 using the modulation depths m_1 and m_2 from Table 1. For the direct detection (LED) experiments this ratio is $m_1/2 = 0.3$, which matches the measured amplitude ratio of 0.3. For the heterodyne with dc offset (laser) experiments, the ratio is $m_1 m_2/4 = 0.0875$, which agrees well with the large amplitude ratio of 0.1 from Fig. 7. Thus these measurements also match theoretical calculations.

3.5 LED 3 frames per cycle noise results

According to theoretical calculations noted in the Table 9 of the appendix, three frames per cycle is a special case in which the AC and phase noise can deviate from the theoretical shot noise values by up to 15%. The experimental noise measurements were taken at high DC amplitudes with some noise removed. Figure 8 shows the theoretical and measured AC and phase noise values.

The measured AC noise values follow the sinusoidal trend of the theoretical values but do not reach the precise values for reasons unknown. The phase noise values follow the

#146883 - $15.00 USD Received 2 May 2011; revised 13 Jun 2011; accepted 13 Jun 2011; published 15 Jun 2011

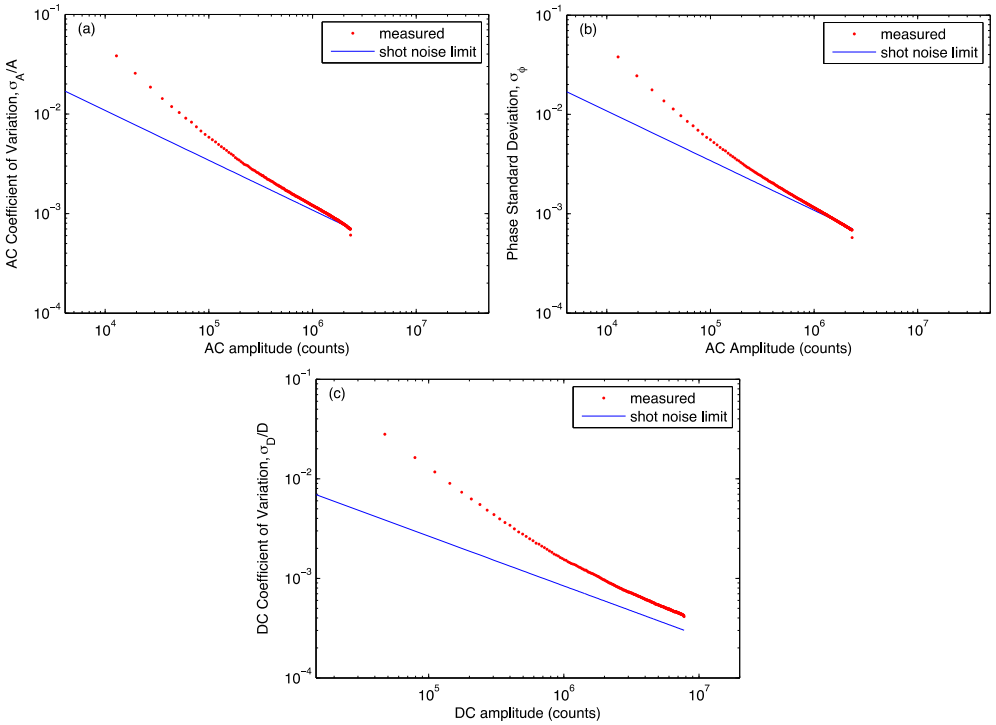

Fig. 5. Measured vs theoretical noise from the LED system from images with 1000 frames and 20 LED cycles. The x axes for Figs. 5-7 are total counts summed over all frames (1000 frames for this figure). Note that the AC CV (coefficient of variation) and phase standard deviation are almost identical. The best measured phase noise is 0.0007 radians or 0.04 degrees.

theoretical values nearly perfectly. With the upper and lower bounds of the AC and phase noise values deviating from the norm at 15%, imaging at three frames per cycle is possible with predictable noise ranges.

4. Conclusions

We have demonstrated that optical and frequency domain imaging can be performed utilizing a high speed camera and FPGA system with total imaging times as short as 3 ms. For these imaging modalities, usually two of the three (DC, AC, phase) measurements are required for subsequent analysis, although all three must be calculated initially. With both the LED and laser systems, DC measurements have more noise than AC and phase measurements. A shot-noise limited system is desired because it means that the system itself introduces no noise into the measurements.

The experiment setup with the LED has been shown to be shot-noise limited and to maintain good linearity for data sets involving 3 frames to 1000 frames. Measurements taken over 1 second have good AC and phase shot-noise limited characteristics, while DC noise measurements have slightly more noise and do not match the theoretical shot-noise values. In addition, these measurements maintain accurate and precise linearity when imaged with a frame rate of 1000 Hz with LED waveforms at 50, 100, and 200 Hz (5, 10, and 20 frames per cycle) with residuals at or below 0.03. Measurements imaged at 250 Hz (4 frames per cycle) with phase variation of the illumination waveform, α, have slightly worse linearity characteristics, presumably due to source intensity nonlinearities.

Images taken at speeds below 10 ms have good DC, AC and phase noise characteristics and follow the shot-noise limitations. Measurements at these fast speeds also have good

#146883 - $15.00 USD Received 2 May 2011; revised 13 Jun 2011; accepted 13 Jun 2011; published 15 Jun 2011

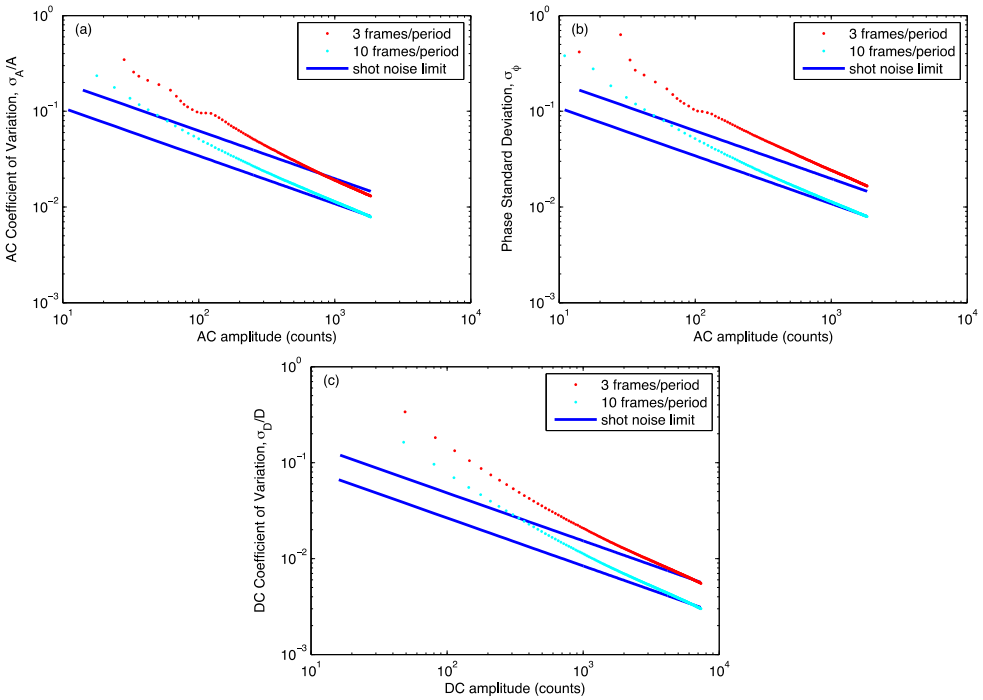

Fig. 6. Measured vs theoretical noise from the LED system from images with 3 and 10 frames and 1 LED cycle. Note that the AC CV and phase standard deviation deviate for large amplitude with 3 frames per cycles—this effect is elucidated in Fig. 8.

linearity characteristics with residuals below 0.02 (aside from images taken at 9 ms). Images taken with 3 frames at a frame rate of 1000 Hz (3 ms) have special noise characteristics that agree with theoretical expressions.

The experiment setup shown in Fig. 3 with the laser and image intensifier has shown to be near shot-noise limited and good linearity characteristics. Measurements were taken with a frame rate of 400 Hz over 1 second with waveforms at 20 Hz and had a residual of 0.34. AC and phase noise characteristics were limited to 2-3 times the shot-noise limitations while DC noise characteristics were many times above that. Therefore, for these types of measurements, AC and phase should be used.

Consistent throughout these experiments was the fact that the DC measurements tended to have more noise than the AC and phase measurements. This may be attributed to the 1/f noise inherent in modulating waveforms, the instability of the image intensifier for the laser setup, or the imprecision of the DAQ digital output. The effective area of the phosphor screen in the image intensifier was unstable and diminished over time, which may contribute to the amount of noise.

These results show that our system can be used for optical and frequency domain imaging at speeds ranging from 3 ms to 1 s with good linearity and noise characteristics.

Appendix A: Measurement uncertainties from shot noise for frequency domain measurements

We are considering the noise for frequency domain measurements involving detecting light with periodic intensity modulation. This can encompass a variety of situations including photon migration measurements involving detection of the attenuation of the primary light source or fluorescent light, fluorescence lifetime imaging microscopy, or time resolved

#146883 - $15.00 USD Received 2 May 2011; revised 13 Jun 2011; accepted 13 Jun 2011; published 15 Jun 2011

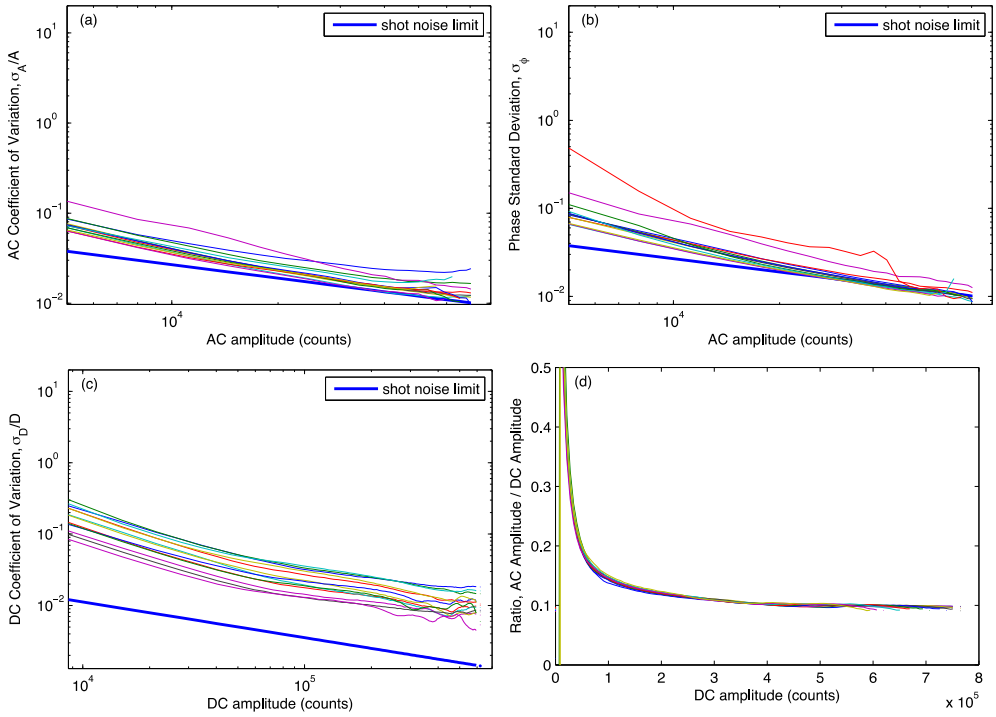

Fig. 7. Measured vs actual noise from image intensifier system with 400 frames and 20 cycles. AC/DC ratios vs DC amplitude. Different colors indicate different phase shifts.

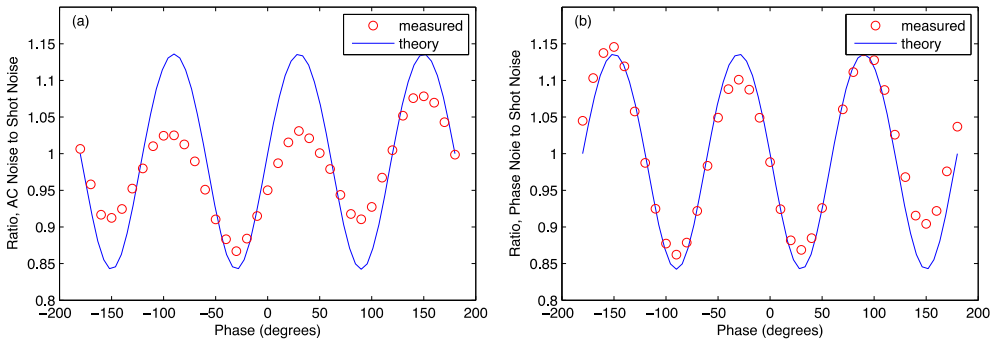

Fig. 8. Measured and theoretical AC noise ratios per phase taken with phase increments of 10 degrees.

ranging measurements. The measurements typically are performed as two quadratures, which we will write as X and Y as they would be represented on the polar plane. These can be determined from the real and imaginary parts of Fourier transformed data or from cosine and sine correlations. The modulated (AC) amplitude A and phase ϕ are given by Eqs. (2) and (3) above. Standard error propagation using Eqs. (2) and (3) gives the dimensionless expressions for the coefficient of variation in the AC amplitude and phase uncertainty [Eq. (4) and Eq. (5)]

$$\frac{\sigma_A^{\,2}}{A^2} = \frac{\cos^2(\phi)\sigma_X^{\,2} + \sin^2(\phi)\sigma_Y^{\,2} + \sin(2\phi)\sigma_{XY}^{\,2}}{A^2}, \tag{4}$$

$$\sigma_\phi^{\,2} = \frac{\sin^2(\phi)\sigma_X^{\,2} + \cos^2(\phi)\sigma_Y^{\,2} - \sin(2\phi)\sigma_{XY}^{\,2}}{A^2}, \tag{5}$$

#146883 - $15.00 USD Received 2 May 2011; revised 13 Jun 2011; accepted 13 Jun 2011; published 15 Jun 2011

where σ_X^2 and σ_Y^2 are the variances in X and Y, and σ_{XY} is the covariance in X and Y. In the following we will consider only the case where the noise is determined by shot noise, which constitutes a fundamental limit governed by the number of detected photons, except with methods such as squeezed light [15]. While there have been several examinations of shot noise for frequency domain measurements [6,16,17], these typically provide scaling relations only and do not consider different types of frequency domain measurements. Here we derive expressions for amplitude coefficients of variation and phase noise for several frequency domain detection methods in the shot noise limit. The number of photoelectrons produced on the detector depends on many factors including the intensity of the light source, the quantity and fluorescence cross sections of any fluorophors involved, propagation losses between the light source and detector, filter transmission efficiency, detection solid angle, and detector quantum efficiency. These details vary by application. However, it is only the number of photoelectrons produced in the detector, which could be a photocathode, photodiode, or camera pixel, that influence the shot noise, so we begin with the number of photoelectrons produced. If the light is modulated at a frequency, ω_1, phase, α, and modulation efficiency, m_1, then $N_{\Delta t}$, the average number of photoelectrons produced in a measurement time Δt centered at time t is

$$N_{\Delta t}(t) = \frac{i_{dc}\Delta t}{q}\left[1 + m_1 \cos(\omega_1 t + \alpha)\right] \tag{6}$$

with $m_1 \le 1$. Note that the dc level $i_{dc}/q\ \Delta t$ includes all dc light whether from the frequency domain light source or background light, whereas the modulated light ($i_{dc}\ \Delta t\ /q$) $m_1\cos(\omega_1 t+\alpha)$] is predominantly from the frequency domain light source. For shot noise, the average fluctuation in this value is

$$\sigma_{N\Delta t}(t) = \sqrt{N_{\Delta t}(t)} = \sqrt{\frac{i_{dc}\Delta t}{q}\left[1 + m_1 \cos(\omega_1 t + \alpha)\right]}. \tag{7}$$

In general two steps are involved in determining the amplitude and phase from the photoelectrons in Eqs. (6) and (7): first electrical gain, possibly with electrical modulation and second, conversion to quadrature values. If the electrical signals are amplified and modulated by a time varying factor E(t), the detected signal and noise become

$$S_{\Delta t}(t) = N_{\Delta t}(t)E(t), \tag{8}$$

$$\sigma_S(t) = \sqrt{N_{\Delta t}(t)}E(t), \tag{9}$$

where $E(t)$ includes a factor to convert electrons to a measurable value such as volts or counts. A single quadrature X is found by correlation of the signal from Eq. (8) with a cosine function according to

$$X = \int_{-T/2}^{T/2} S(t)\cos(\omega t + \gamma)dt = \int_{-T/2}^{T/2} N_{\Delta t}(t)E(t)C(t)dt. \tag{10}$$

Integrals for the other quadrature, Y, and the DC, D, are the same as Eq. (10) except with $C(t)$ replaced by $S(t)$ and 1, respectively. $C(t)$ and $S(t)$ are of the general form $\cos(\omega t+\gamma)$ and $\sin(\omega t+\gamma)$. Although we write the expressions for the two quadratures as correlations, the following analysis is valid for calculation of the quadratures through Fourier transforms as well because the two correlations for X and Y are identical to the real and imaginary parts of the Fourier transform, with the exception of a constant multiplier. The constant multiplier does not affect the dimensionless noise expressions in Eqs. (4) and (5).

While the signal adds linearly in Eq. (10), the noise adds in quadrature. That is, the variance in each quadrature is found by summing the variance for each time interval, which is given by the square of Eq. (9) times the square of the multiplicative factor, $C(t)$ or $S(t)$. We write the summed variance as an integral according to

#146883 - $15.00 USD Received 2 May 2011; revised 13 Jun 2011; accepted 13 Jun 2011; published 15 Jun 2011

$$\sigma_x^{\,2} = \int_{-T/2}^{T/2} \sigma_{N\Delta t}^{\,2}(t)\left[E(t)\right]^2\left[C(t)\right]^2 dt = \int_{-T/2}^{T/2} N_{\Delta t}(t)\left[E(t)\right]^2\left[C(t)\right]^2 dt. \qquad (11)$$

Expressions for $\sigma_Y^{\,2}$, $\sigma_D^{\,2}$ and σ_{XY} are the same as Eq. (11) except that $[C(t)]^2$ is replaced with $[S(t)]^2$, 1, and $C(t)S(t)$ respectively. This analysis is valid regardless of whether the experiment is better described by an integral such as Eqs. (10), or by summations such as in Eq. (1); i.e., by either continuous or discrete correlations or Fourier transforms.

There are a variety of detection methods for frequency domain measurements that differ in the manner of demodulation as summarized in Table 5. Each has distinct parameters for $E(t)$, $C(t)$, and $S(t)$, which are given in Table 6. The AC may be separated from the DC using filters prior to electronic demodulation and digitization of the signal (Cases 1A and 1B) or the AC and DC may be digitized together (Cases 2A and 2B). The homodyne methods perform demodulation in one step to determine the quadratures X and Y, such as performing RF mixing with an I/Q demodulator to produce two DC quadratures (Case 1A) or demodulation computationally following digitization (Case 2A). Heterodyne methods perform demodulation in two steps with a first mixing step reducing an RF frequency ω_1 to a lower (intermediate) frequency $|\omega_1-\omega_2|$ and a second step to determine the quadratures X and Y. Measurements with a photomultiplier typically perform the heterodyne and digitization of the AC separately from the DC (Case 1B), while measurements using an image intensifier perform the heterodyne without AC/DC separation and digitize AC and DC together (Case 2B).

Table 5. Cases considered for frequency domain measurements

	Homodyne	Heterodyne
Separated DC/AC	Case 1A: Homodyne	Case 1B: Heterodyne
Combined DC/AC	Case 2A: Direct Detection	Case 2B: Heterodyne with DC Offset

Substituting the terms in Table 6 into Eqs. (10) and (11) and using Eqs. (4) and (5) gives the expressions for the signal and variance in Table 7 and the dimensionless noise expressions in Table 8, where $N = i_{dc}T/q$. These expressions are valid when all of the oscillatory terms average to zero (well-sampled conditions). The covariance σ_{XY} is zero for well-sampled conditions. When the number of intervals is small or the integration range does not cover an integral number of cycles of the various difference frequencies, then the results will differ somewhat from the expressions in Table 8, as is described below for three measurements per

Table 6. Electrical modulation and analysis demodulation terms for different frequency domain measurement types

	DC Electrical Term $E_{DC}(t)$	AC Electrical Term $E_{AC}(t)$	Analysis Terms $C(t)$, $S(t)$
Case 1A: Homodyne	G	$G\cos(\omega_1 t + \beta)$ for X $G\sin(\omega_1 t + \beta)$ for Y	1 1
Case 1B: Heterodyne	G	$G\cos(\omega_2 t + \beta)$	$\cos[(\omega_1-\omega_2)t + \gamma]$ $\sin[(\omega_1-\omega_2)t + \gamma]$
Case 2A: Direct Detection	G	G	$\cos(\omega_1 t + \gamma)$ $\sin(\omega_1 t + \gamma)$
Case 2B: Heterodyne with DC Offset	$G\,[1 + m_2\cos(\omega_2 t + \beta)]$	$G\,[1 + m_2\cos(\omega_2 t + \beta)]$	$\cos[(\omega_1-\omega_2)t + \gamma]$ $\sin[(\omega_1-\omega_2)t + \gamma]$

Table 7. Signal and variance for different types of frequency domain measurements

	DC Signal D	DC Variance $\sigma_D^{\,2}$	Single Quadrature Signal X, Y	Single Quadrature Variance $\sigma_X^{\,2}$, $\sigma_Y^{\,2}$
Case 1A: Homodyne	GN	G^2N	$(GNm_1/2)\cos(\beta-\alpha)$ $(GNm_1/2)\sin(\beta-\alpha)$	$G^2N/2$ $G^2N/2$
Case 1B: Heterodyne	GN	G^2N	$(GNm_1/4)\cos(\beta+\gamma-\alpha)$ $(GNm_1/4)\sin(\beta+\gamma-\alpha)$	$G^2N/4$ $G^2N/4$
Case 2A: Direct Detection	GN	G^2N	$(GNm_1/2)\cos(\gamma-\alpha)$ $(GNm_1/2)\sin(\gamma-\alpha)$	$G^2N/2$ $G^2N/2$
Case 2B: Heterodyne with DC	GN	$G^2N\,(1 + m_2^{\,2}/2)$	$(GNm_1m_2/4)\cos(\beta+\gamma-\alpha)$ $(GNm_1m_2/4)\sin(\beta+\gamma-\alpha)$	$(G^2N/2)(1 + m_2^{\,2}/2)$ $(G^2N/2)(1 + m_2^{\,2}/2)$

#146883 - $15.00 USD Received 2 May 2011; revised 13 Jun 2011; accepted 13 Jun 2011; published 15 Jun 2011

cycle for Case 2A. Note that the expressions in Table 8 depends only N, m_1, and m_2. The gain or conversion factor G cancels out. G can be different for the AC and DC signals without affecting the dimensionless noise expressions.

The difference between the various expressions in Table 8 can be understood as follows. First, for the dimensionless DC noise, the expressions for σ_D /D in Cases 1A, 2A, and 1B are all the same and equal to the expected expression for shot noise, $N^{-1/2}$. For Case 2B, the DC uncertainty increases by an additional factor of $(1+m_1^2/2)^{1/2}$ relative to the signal, which arises because the signal sums linearly while the noise sums in quadrature, resulting in an increase of the noise relative to the signal. The dimensionless AC noise terms σ_ϕ and σ_A /A are always larger than the dimensionless DC noise terms for two reasons. First, a non-unity modulation depth leads to a reduction in the AC signal relative to the DC signal while the noise is unaffected by the modulation depth, resulting in a net increase in the dimensionless AC noise by a factor of $1/m_1$ for Cases 1A/2A/1B or $1/(m_1m_2)$ for Case 2B. Second, each demodulation step leads to an increase in the dimensionless AC noise by a factor of $2^{1/2}$ because the oscillatory sampling reduces both the AC signal and the AC variance by a factor of two relative to their nominal amplitudes, and the dimensionless noise scales with the square root of the variance. This leads to a net factor of $2^{1/2}$ or 2 increase in the dimensionless AC noise for Cases 1A/2A or Case 1B, which have one and two demodulation steps, respectively. For case 2B the net increase is $2(2^{1/2})$ because the first demodulation step passes the full DC noise. Note that the dimensionless noise expressions for the two homodyne methods (Case 1A and Case 2A) are identical.

Table 8. Dimensionless noise expressions for different types of frequency domain measurements

	σ_D/D	σ_ϕ or σ_A/A
Case 1A: Homodyne	$(1/N)^{1/2}$	$(1/m_1)(2/N)^{1/2}$
Case 1B: Heterodyne	$(1/N)^{1/2}$	$(2/m_1)(1/N)^{1/2}$
Case 2A: Direct Detection	$(1/N)^{1/2}$	$(1/m_1)(2/N)^{1/2}$
Case 2B: Heterodyne with DC Offset	$[(1 + m_2^2/2)/N]^{1/2}$	$[2/(m_1m_2)][(2 + m_2^2)/N]^{1/2}$

Derivation of the expressions for the variances in Table 8 can also proceed through a Fourier transform based analysis, noting that shot noise is white noise. The Fourier transform of the mean square fluctuations are given by the autocorrelation of the noise fluctuations. For white noise, the autocorrelation function is only a delta function at zero delay, which is equivalent to the DC integral of the noise variance. In essence, the noise spectrum is flat with equal noise power at every frequency. However, for the AC calculations, the noise power is equally split into the real and imaginary parts, or two quadratures. These are the Fourier transforms of the even and odd parts of the noise fluctuations and the noise is equally composed of each. Thus we see from Table 8 that the AC noise variance terms are equal to half of the DC noise variance for Cases 1A, 2A, and 2B. For Case 1B, there is a factor of four difference in noise variance. One factor of two is due to the heterodyne modulation that is applied to the AC signal only. The second factor of two is due to the separation into two quadratures. In the closest analysis to ours, Toronov et al. [6] have analyzed the noise scaling for Case 2B, although their expression for the AC amplitude and phase noise has m_2 only where ours has m_2^2.

The expressions in Eqs. (2), (3) and (10) and Tables 7 and 8 are valid when all oscillatory terms integrate to zero (well sampled conditions). Well-sampled conditions are well fulfilled though not exact when many measurements span a large number of periods of the light source $\tau = 2\pi/\omega_1$. Well-sampled conditions are exactly fulfilled even for a single period τ for Cases 1A and 2A (and also Cases 1B and 2B provided low pass filtering removes the $\omega_1+\omega_2$ frequency) or when there are n_p evenly spaced measurements per period τ (i.e., measurements are τ/n_p apart) and $n_p \geq 4$. Two measurements are sufficient to determine A and ϕ when the DC contribution to the measurements is zero, but not for evenly spaced measurements because only one quadrature is sampled. For n_p=3 and even sample spacing, Eqs. (2), (3) and (10) are correct, but the expressions for the AC and phase noise parameters in Tables 7 and 8 are not

#146883 - $15.00 USD Received 2 May 2011; revised 13 Jun 2011; accepted 13 Jun 2011; published 15 Jun 2011

valid because there is a correlation between the noise expression of Eq. (7) and the sampling spacing τ/3, and the terms with frequency $3\omega_1$ resulting from Eq. (11) do not sum to zero. Correct AC noise expressions for n_p=3 with even sample spacing for Cases 1A and 2A are shown in Table 9. The dimensionless phase and amplitude noise σ_ϕ and σ_A /A depend on the phase of the light α when the measurements are performed, as verified experimentally in Figure 8.

Table 9. Expressions for Cases 1A and 2A with three evenly spaced measurements per modulation cycle (n_p = 3).

σ_X^2, σ_Y^2	σ_{XY}	σ_ϕ, σ_A/A
$(G^2N/2)[1 + (m_1/2)\cos(\alpha + 2\beta)]$ $(G^2N/2)[1-(m_1/2)\cos(\alpha + 2\beta)]$	$(G^2Nm_1/4)\sin(\alpha + 2\beta)$	$(1/m_1)\{[2-m_1\cos(3\alpha)]/N\}^{1/2}$ $(1/m_1)\{[2 + m_1\cos(3\alpha)]/N\}^{1/2}$

Acknowledgments

This work was supported by a Major Research Instrumentation grant from the National Science Foundation (NSF), by the NSF Research Experiences for Undergraduates Program, and by SRI International. We acknowledge additional contributions from Sanhita Dixit (system testing), John Binder (fiber interface board design), Nevena Rakuljic, Kenneth T. Kotz, David Manseau, and Abneesh Srivastava (initial RF and intensifier circuitry) and Kameron Harmon (initial graphical user interface).

#146883 - $15.00 USD Received 2 May 2011; revised 13 Jun 2011; accepted 13 Jun 2011; published 15 Jun 2011